


Article

Mutated Human P-Selectin Glycoprotein Ligand-1 and Viral Protein-1 of Enterovirus 71 Interactions on Au Nanoplasmonic Substrate for Specific Recognition by Surface-Enhanced Raman Spectroscopy

Kundan Sivashanmugan ^{1,2}, Han Lee ¹, Jiunn-Der Liao ^{1,3,*}, Chen-Chu Wang ⁴,
Chen-Hsueh Lin ¹, Yuh-Shyong Yang ⁴  and Jaya Sitjar ¹

¹ Department of Materials Science and Engineering, National Cheng Kung University, Tainan 70101, Taiwan; sivashanmugannst87@gmail.com (K.S.); rick594007@hotmail.com (H.L.); az436436@gmail.com (C.-H.L.); jaya.sitjar@gmail.com (J.S.)

² School of Electrical Engineering and Computer Science, Oregon State University, Corvallis, OR 97331, USA

³ Medical Device Innovation Center, National Cheng Kung University, 1 University Road, Tainan 70101, Taiwan

⁴ Department of Biological Science and Technology, National Chiao Tung University, Hsinchu 30010, Taiwan; rick594007@yahoo.com.tw (C.-C.W.); ysyang@faculty.nctu.edu.tw (Y.-S.Y.)

* Correspondence: jdliao@mail.ncku.edu.tw; Tel.: +886-6-2757575 (ext. 62971); Fax: +886-6-2346290

Received: 29 February 2020; Accepted: 14 April 2020; Published: 19 April 2020



Abstract: Protein tyrosine sulfation is a common post-translational modification that stimulates intercellular or extracellular protein-protein interactions and is responsible for various important biological processes, including coagulation, inflammation, and virus infections. Recently, human P-selectin glycoprotein ligand-1 (PSGL-1) has been shown to serve as a functional receptor for enterovirus 71 (EV71). It has been proposed that the capsid viral protein VP1 of EV71 is directly involved in this specific interaction with sulfated or mutated PSGL-1. Surface-enhanced Raman spectroscopy (SERS) is used to distinguish PSGL-1 and VP1 interactions on an Au nanoporous substrate and identify specific VP1 interaction positions of tyrosine residue sites (46, 48, and 51). The three tyrosine sites in PSGL-1 were replaced by phenylalanine (F), as determined using SERS. A strong phenylalanine SERS signal was obtained in three regions of the mutated protein on the nanoporous substrate. The mutated protein positions at (51F) and (48F, 51F) produced a strong SERS peak at 1599–1666 cm^{-1} , which could be related to a binding with the mutated protein and anti-sulfotyrosine interactions on the nanoporous substrate. A strong SERS effect of the mutated protein and VP1 interactions appeared at (48F), (51F), and (46F, 48F). In these positions, there was less interaction with VP1, as indicated by a strong phenylalanine signal from the mutated protein.

Keywords: P-selectin glycoprotein ligand-1; viral protein 1; surface-enhanced Raman spectroscopy; nanoporous; phenylalanine

1. Introduction

Protein tyrosine sulfation (PTS) is a significant post-translational modification that occurs via the tyrosyl protein sulfotransferase (TPST) catalyst through the transfer of the sulfonyl group (SO_3^-) from 3'-phosphoadenosine-5'-phosphosulfate, resulting in the addition of a specific tyrosyl residue within a target protein [1–4]. PTS is of vital importance as it facilitates protein-protein interactions (PPIs), which regulate many biological events, such as virus infection, inflammation, immune responses, and physiological and pathological diseases [3,5–8]. Notably, the pathogenic mechanism can be

evaluated via the activity of PTS. PTS facilitates and controls the chemokine receptor-ligand binding, which is relevant in inflammatory responses [5,9–13]. PTS-based PPIs have potential for disease treatment via a target protein. Mutated tyrosine residues in CC chemokine receptor 5 strongly reduce human immunodeficiency virus-1 infection (50%–70%) when compared to control residues [10,14]. Monitoring PTS activity in PPIs is essential for recognizing and understanding biological functions and mechanisms.

Enterovirus 71 (EV71) is a non-enveloped positive-stranded RNA virus composed of four structural proteins (VP1, VP2, VP3, and VP4) [15,16]. It belongs to the picornaviridae family, which produces agents that are responsible for hand, foot, and mouth disease [15,16]. In addition, there is no effective antiviral agent known to be effective in treating EV71 infection. Notably, P-selectin glycoprotein ligand-1 (PSGL-1) is a functional receptor for EV71 [15]. PSGL-1 is primarily expressed on the surface of circulating leukocytes, where it mediates platelet rolling and inflammatory processes [15,16]. The N-terminal tyrosine sulfation of PSGL-1 is crucial for the binding of specific strains of EV71 through its capsid protein (VP1), which enables virus infection [15,16]. The three key tyrosine residue sulfation specific positions at 46, 48, and 51 are placed on the PSGL-1 terminal [3,4,17]. During PPIs, it is difficult to clearly distinguish the specific positions of PTS sites in VP1 interactions, and the process is time-consuming. PPIs greatly affect the function and structure of proteins and change the regulation of the target protein. Thus, it is important to investigate PPIs for commercial drug design.

Many characterization methods have been applied to monitor PTS-based PPIs, including mass spectrometry, western blotting, and enzyme-linked immunosorbent assays [18–20]. These methods usually require tedious sample preparation and expensive instruments. Moreover, the specific monitoring of PTS-based PPIs requires a long time and a high concentration due to the instability of sulfated target proteins in real-time applications. Therefore, rapid, simple, and quantitative methods are needed for monitoring PTS-based PPIs. In addition, a fluorescence method has been used to monitor PTS via phenol sulfotransferase-TPST coupled enzyme assay substrates [4,17]. Atomic force microscopy (AFM) can be employed to qualitatively and quantitatively characterize single-molecule interactions with a very high spatial resolution. In our earlier work, AFM was used to measure the unbinding force between sulfated or mutated PSGL-1 and VP1 *in vitro* [21]. It was found that the binding strength increased following PTS treatment on PSGL-1 with a specific anti-sulfo tyrosine antibody and VP1 protein of EV1. Moreover, the tyrosine-51 residue of glutathione S-transferases fusion-PSGL-1 (GST-PSGL-1) has less affinity compared to other tyrosine residues towards the VP1 protein of EV1. Raman spectroscopy can be used to analyze bio-species with or without a solution state; however, weak Raman signals and limited information are obtained [22,23]. Surface-enhanced Raman spectroscopy (SERS) can be used to investigate bio-species via Raman-active modes [24–29]. Detection mainly involves a chemical effect and an electromagnetic (EM) effect [24,30–32]. Chemical specificity and high sensitivity can be obtained via the SERS effect [24]. Generally, substrates roughened using metal (Au, Ag) nanoparticles or patterned nanostructures are used to investigate bio-species, with a high SERS effect and a high enhancement factor [25–27]. The SERS effect strongly depends on the geometry of NSs in the micro-environment. Size-based bio-species characterization requires a large SERS effect and reproducibility.

The present work utilizes the SERS technique to investigate the interactions between sulfated or mutated GST-PSGL-1 and an antibody or VP1 of EV71 on a nanoplasmonic surface. The high-purity tyrosine sulfation residues were obtained by using the GST fusion tag without affecting TPST activity on GST-PSGL-1. Figure 1 shows the experimental design of GST-PSGL-1 and the mutants of GST-PSGL-1. The three tyrosine residues of GST-PSGL-1 (at positions 46, 48, and 51) were mutated via substitution by phenylalanines (F). We investigated sulfated (S) or mutated GST-PSGL-1 and VP1 protein of EV71 interactions and the interaction position of tyrosine residues via SERS spectral changes on an Au nanoporous surface in real time. The SERS spectra were used to determine whether the GST-PSGL-1 and VP1 interactions at the three tyrosine residues had different activity abilities after being subjected to PTS.

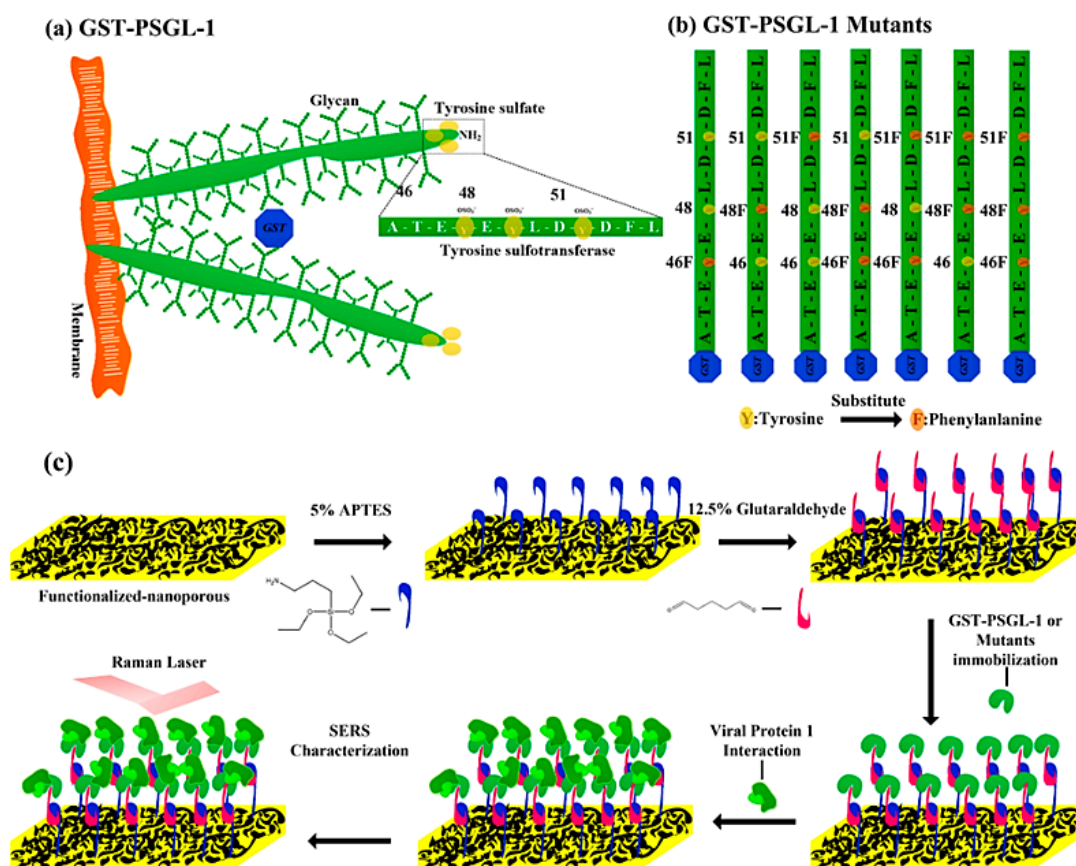


Figure 1. (a) The basic structure of the glutathione S-transferases fusion-human P-selectin glycoprotein ligand-1 (GST-PSGL-1) protein and (b) experimental design of the mutated GST-PSGL-1 protein purified are presented using GST fusion. (c) A schematic illustration of the experimental process for protein-protein interactions (PPIs) on the Au nanoplasmonic substrate is shown.

2. Experimental Section

2.1. Fabrication of the Au Nanoporous SERS Substrate

Various kinds of nanoporous surface have been fabricated in previous studies [33–37]. The high density and uniformity of Au nanoporous substrates make them suitable as SERS substrates. In this work, Au nanoporous substrates were fabricated using an Ag–Au alloy ($\text{Ag}_{80}\text{Au}_{20}$ at.%) target. Briefly, the experiment started with the deposition of 400-nm-thick Au layers via an electron beam (e-beam) evaporator (VT1-10CE, ULVAC, Tainan, Taiwan) on polished single-crystal silicon (100) wafers primed with a 5-nm-thick adhesion layer of Ti. Then, a 150-nm-thick Ag/Au alloy layer was deposited via e-beam at two deposition rates (0.3 and 1 $\text{\AA}/\text{s}$, respectively). Finally, the Au nanoporous surface was formed by dealloying Ag in concentrated nitric acid at various durations (30–210 s). A bottom thick adhesion layer of Au was deposited to increase the adhesion strength of Ag/Au alloy to the Si substrate to avoid film breakage during dealloying. The sample was washed with deionized (DI) water to remove the dealloying reaction products and excess nitric acid. The morphology, chemical composition, and optical properties of as-prepared samples were investigated using field-emission scanning electron microscopy (FE-SEM, JSM-7001, JEOL, Tokyo, Japan), HR-TEM-EDS (JEM-2100F, JEOL), and ultraviolet-visible spectrophotometry. Water solution contact angles on as-fabricated substrates were measured at 25 $^{\circ}\text{C}$ with an angle meter. A 5- μL droplet of DI water was placed on the sample surface at three sites to assess the surface wettability for measuring the average contact angle.

2.2. Molecular Probe Detection

Rhodamine 6G was diluted in aqueous solution in the range of 10^{-6} to 10^{-12} M. To investigate the SERS effect, the molecular solution was placed on the as-fabricated samples (created at rates of 0.3 and 1 Å/s), and then subjected to Raman spectroscopy. Raman spectra were obtained using a confocal microscopy Raman spectrometer (inVia Raman microscope, Renishaw, London, UK) using a He–Ne laser with an excitation wavelength of 633 nm, a magnification of 50×, and an integration time of 10 s over an area of $1 \mu\text{m} \times 1 \mu\text{m}$ (the size of the laser spot was $\sim 1 \mu\text{m}$). An air-cooled charge-coupled device (CCD) was used as the detector, and the incident power was 3 mW. Before each measurement, the Raman shift was calibrated using the signal at 520 cm^{-1} with the absolute intensity from a standard silicon wafer.

The enhancement factor (EF) was calculated according to the standard equation [25–27]:

$$\text{EF} = \frac{I_{\text{sers}}}{I_{\text{bulk}}} \times \frac{N_{\text{bulk}}}{N_{\text{sers}}} \quad (1)$$

where I_{sers} and I_{bulk} are the SERS and normal Raman scattering intensities, respectively, and N_{sers} and N_{bulk} are the numbers of molecules contributing to the inelastic scattering intensity, respectively, as evaluated by SERS and normal Raman scattering measurements. The SERS effect was averaged from twenty consecutive measurements. The commercial software COMSOL (version Multiphysics® 2019) was applied to calculate the EM field distribution on the Au nanoporous substrates [25,27].

2.3. Protein Immobilization on Plasmonic Au Nanoporous Substrate

2.3.1. Protein Preparation

The protocols used for TPST, PSGL-1, GST-PSGL-1, S-GST-PSGL-1, mutant GST-PSGL-1, and VP-1 of EV71 are explained in our earlier publication [4,17,21]. The following molecular weights were used in this work: NusA-tag fusion protein (60 kDa), TPST (36 kDa), GST-PSGL-1 (27.8 kDa), and VP1 (33 kDa) [21].

2.3.2. Self-Assembled Monolayers of Proteins on Au Nanoporous Substrate

To assemble protein on Au nanoporous substrates, the optimized Au nanoporous substrates were cleaned with acetone for 10 min and then treated with oxygen plasma for 3 min. The treated Au nanoporous surface was soaked in a 2% 3 APTES/ethanol solution for 30 min and then carefully washed with ethanol and heated at $120 \text{ }^\circ\text{C}$ for 10 min to produce amine groups on the surface and remove surplus ethanol. The APTES-modified Au nanoporous surface was then incubated in phosphate-buffered saline (PBS; pH 7) with 12.5% glutaraldehyde for 1 h. The self-assembled monolayer (SAM) that formed on the surface was washed with double-distilled water (ddH_2O) and dried with nitrogen gas. Then, the surface-modified Au nanoporous substrate was immersed in $1 \mu\text{M}$ PBS with GST-PSGL-1 or mutant GST-PSGL-1 peptides for 12 h, respectively. Next, the protein-immobilized Au nanoporous surface was washed with PBS solution and subjected to a PTS reaction for 4 h at $37 \text{ }^\circ\text{C}$, as detailed in our earlier publication [21]. After the PTS reaction, the substrate was washed with PBS solution three times. Finally, the protein-modified Au nanoporous surface was soaked in anti-sulfotyrosine (1:1000 dilution) or $1 \mu\text{M}$ VP-1 in PBS for 12 h, and then unreacted probes were removed with PBS solution and characterized using Raman spectroscopy. The surface compositions of the pristine (Au) and protein-immobilized nanoporous substrates were analyzed using XPS with an Al $\text{K}\alpha$ (1486.6 eV) X-ray source. For the pristine and protein-immobilized nanoporous surfaces, wide-scan C 1s, S 2p, N 1s, O 1s, and Au 4f spectra were collected. The morphology of the SAM surface was investigated using field-emission scanning electron microscopy (FE-SEM) and AFM (Dimension Icon, Bruker, Billerica, MA, USA).

3. Results and Discussion

3.1. Characterization of the Plasmonic Au Nanoporous Substrate

A continuous plasmonic Au nanoporous substrate was fabricated using both physical and chemical methods, as illustrated in Figure S1 in Supplementary Materials. Both methods can be used to precisely tune the plasmonic properties of nanoporous materials. The FE-SEM images in Figure 2a,b show the morphology of a plasmonic Au nanoporous surface. The pore size varied with dealloying time (30–210 s, with samples denoted as Aup_30s, Aup_60s, Aup_90s, Aup_120s, Aup_150s, Aup_180s, and Aup_210s) and thus with the deposition rate (0.3 and 1 Å/s). The Au pore sizes and contact angles are given in Table S1. After dealloying, the composition of the Ag–Au alloy film changed from ~80:20 to ~2:20 at.%, as determined from the energy-dispersive X-ray spectroscopy (EDS) spectra. The Au nanoporous surface had a different distribution of plasmonic porous cavity sizes, which significantly affects the local EM field effect. The deposition rate also influences the mechanical and physical properties of nanoporous materials. In addition, the reduction in contact angle is related to the deposition rate. Figure S2 shows a high-resolution transmission electron microscopy (HR-TEM) image of an optimized Au nanoporous substrate (Aup_120, 1 Å/s). The pore size was 50 ± 2 nm, which creates a strong local EM environment, enabling single-molecule detection [24]. The EDS mappings show the formation of a porous structure. Moreover, a continuous plasmonic Au nanoporous substrate has enhanced optical properties from the visible to near-infrared regions under irradiation, which may provide a high density of SERS hot spots.

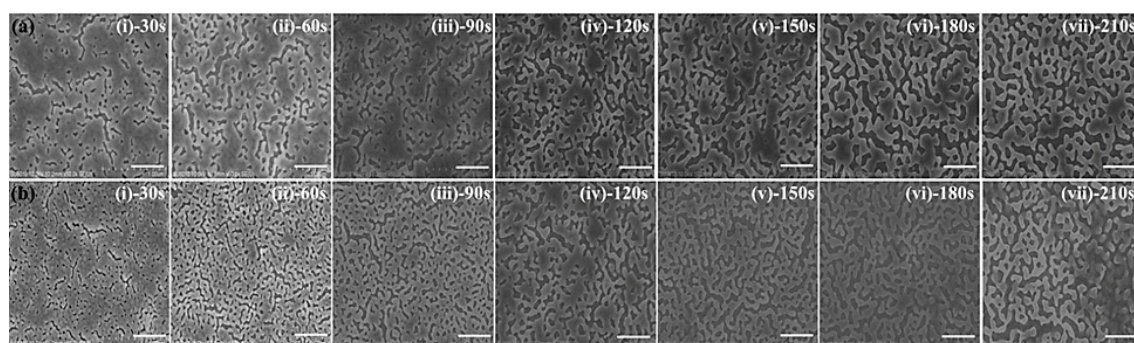


Figure 2. Field-emission scanning electron microscopy (FE-SEM) top-view images of as-fabricated plasmonic Au nanoporous substrates fabricated using deposition rates of (a) 0.3 Å/s and (b) 1 Å/s, and various dealloying durations (scale bar: 500 nm) were present.

The surface plasmon resonance (SPR) spectra of Aup_120s (0.3 and 1 Å/s) and Aup_150s (0.3 and 1 Å/s) substrates are shown in Figure S3. The Ag/Au alloy film SPR peak at 485 nm significantly shifted after the Ag/Au alloy film was dealloyed. Two strong SPR shifts appeared at 681 nm for Aup_150s (1 Å/s) and 735 nm for Aup_120s (1 Å/s) compared to those for a deposition rate of 0.3 Å/s (649 nm for Aup_150s and 688 nm for Aup_120s); these peaks are attributed to the strong multi-polarization electric field coupling in small porous cavities [24–27,33]. COMSOL was used to calculate the optical properties of the optimized Au nanoporous substrate as detailed in SI. We believe that the higher EM field was generated by continuous nanoporous cavities, which allow the detection of lower concentration target species via SERS.

The as-fabricated Au nanoporous samples (30 to 210 s, 0.3 and 1 Å/s) created strong Raman vibrational modes when rhodamine 6G (R6G) was used as the molecular probe. The SERS spectra of 10^{-6} M R6G on as-fabricated Au nanoporous samples were obtained at a laser wavelength of 633 nm, as shown in Figure 3a,b. A strong R6G SERS characteristic peak (I_{SERS}) was obtained at 1363 cm^{-1} for all samples and corresponds to the $\nu(\text{C}=\text{C})$ aromatics mode [26]. The large local EM field enhancement was found in the nanoporous cavity zone, which may allow for multipolar excitations and enhanced Raman scattering. In addition, the matched Raman laser energy with the nanoporous SPR band can

enhance the maximum SERS response. Sample Aup_120s (1 Å/s) had an increased SERS intensity due to its optimal spacing between porous cavities, as shown in Figure 3c. The enhancement factor (EF) was calculated using Equation (1); the optimized Au nanoporous substrate Aup_120s (1 Å/s) obtained enhancement in the order of 10^7 , using the relatively strong band at 1363 cm^{-1} , and was thus used for further studies. The SERS peak intensity at 1363 cm^{-1} for an R6G concentration of 10^{-7} to 10^{-12} M was examined on the optimized Au nanoporous sample, as shown in Figure 3d. The optimized Au nanoporous substrate had a strong SERS intensity due to multipolar enhancement, making it suitable for detection at the single-molecule level. The SERS spectra of R6G were enhanced greatly and equally at each 20 point sampling position on the Au nanoporous substrate, indicating good activity and reproducibility of the sample.

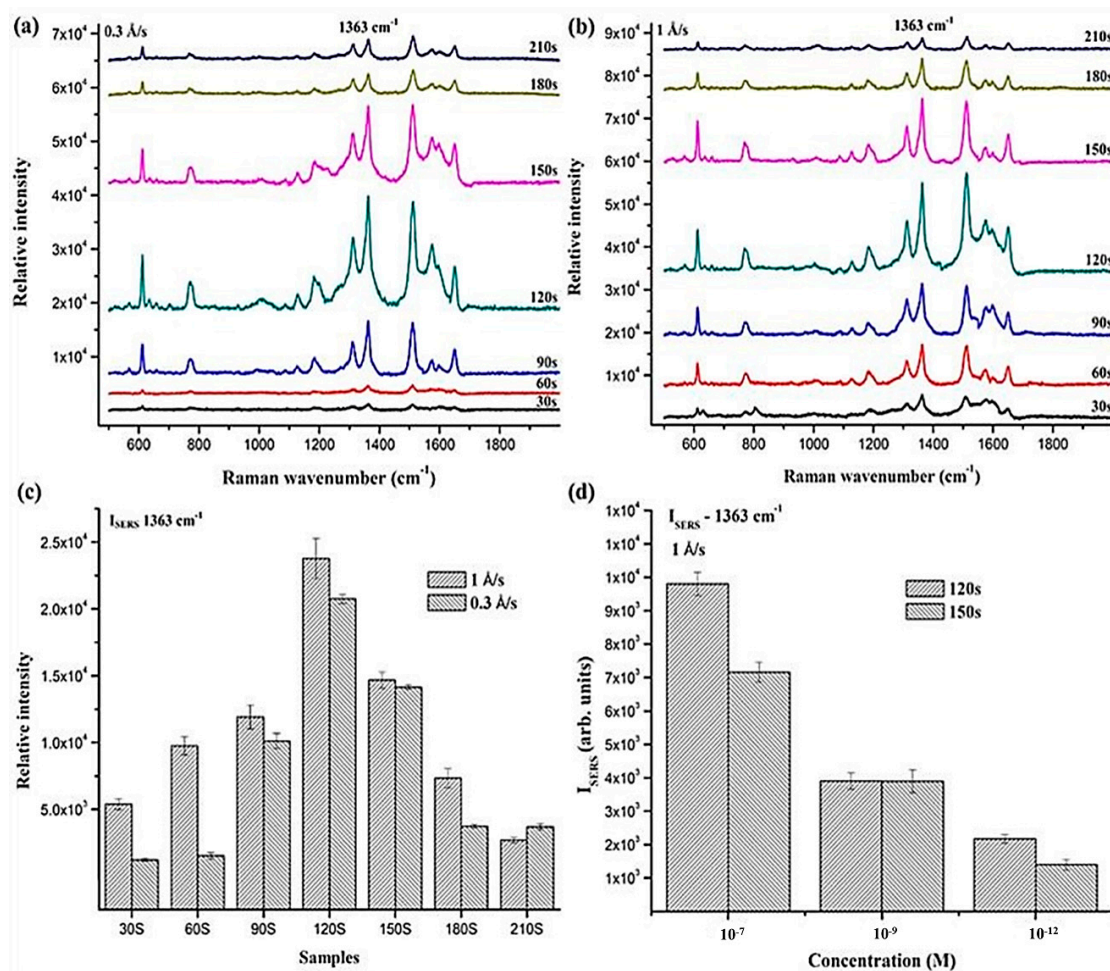


Figure 3. Surface-enhanced Raman spectroscopy (SERS) spectra of 10^{-6} M R6G molecule on as-fabricated Au nanoporous substrates with the deposition rates of (a) 0.3 and (b) 1 Å/s were taken with different dealloying times and examined at a Raman laser wavelength of 633 nm. (c) The SERS characteristic peak at 1363 cm^{-1} was present with intensities for various deposition rates and dealloying times. (d) The SERS spectra of R6G molecules (10^{-7} , 10^{-9} , and 10^{-12} M) on an optimized Au nanoporous substrate were examined at a Raman laser wavelength of 633 nm. The relationship of relative Raman intensities with the concentration of the R6G molecule on an optimized Au nanoporous substrate was shown using I_{SERS} peaks at 1363 cm^{-1} .

3.2. Chemisorption of Protein-Immobilized Plasmonic Au Nanoporous Substrate

The active peptide (ATEYEYLDYDFL)-containing sulfation site of GST-PSGL-1 was immobilized on the functionalized Au nanoporous surface by 3-amino-propyltriethoxysilane (APTES) and glutaraldehyde as linker molecules. The protein immobilization process was confirmed using

X-ray photoelectron spectroscopy (XPS) and SERS characterization. The XPS spectra of C 1s, O 1s, N 1s, S 2p, and Au 4f are shown in Figure 4a–e.

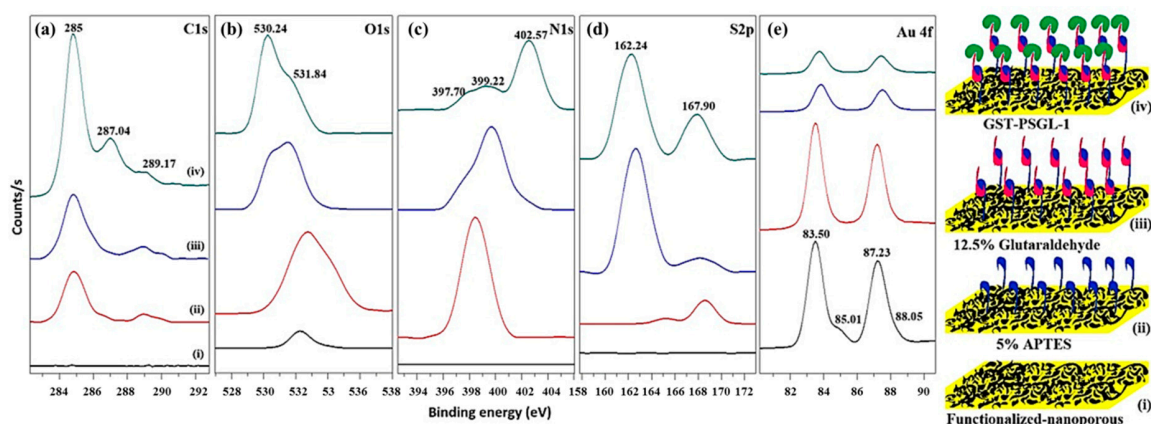


Figure 4. The XPS spectra of protein immobilization on the Au nanoporous substrate were characterized. (a) C 1s, (b) O 1s, (c) N 1s, (d) S 2p and (e) Au 4f spectra were respectively present for verifying chemical components on the Au nanoporous substrate.

For the functionalized Au nanoporous surface with oxygen plasma treatment, the AuO_x spectrum exhibited a weak signal peak at binding energies of 85.01 and 88.05 eV, which confirms the formation of O and OH on the Au nanoporous surface, and SAM formation [38,39]. The Au 4f_{5/2} and Au 4f_{7/2} spectra exhibited strong signal peaks at 83.50 and 87.23 eV, respectively. The peak intensity decreased after protein assembly on the surface due to multi-SAM formation. The O 1s spectrum of the functionalized Au nanoporous surface exhibited an emission peak at 532.24 eV, which indicates the formation of a nano-sized oxidation layer [38]. For the APTES-modified Au nanoporous surface, the C 1s spectrum exhibits strong emission peaks at 284.78 and 288.96 eV, which correspond to C–C and O–C=O, respectively [21,27,40]. The O 1s spectrum of the APTES-modified Au nanoporous surface exhibits a strong emission peak at 532.73 eV, which corresponds to O–C=O from the APTES layer. The N 1s spectrum of the APTES-modified Au nanoporous surface exhibits a strong emission peak at 398.45 eV, which corresponds to NH₂ from the APTES layer. The glutaraldehyde-modified Au nanoporous surface C 1s spectrum exhibits an emission peak at 288.96 eV, which corresponds to H–C=O; these results confirm the chemisorption of glutaraldehyde [21]. The O 1s and N 1s spectra of the glutaraldehyde-modified Au nanoporous surface are similar to those obtained for the APTES-modified surface. The XPS peaks at 287.04 and 289.17 eV for C 1s are from the immobilized GST-PSGL-1 on the Au nanoporous surface, which correspond to C–N, H–C=O, and C=O–N, respectively [21,40]. The disappearing glutaraldehyde H–C=O peak at 288.96 eV confirms the immobilization of the proteins. The XPS peaks in the O 1s spectrum from the immobilized GST-PSGL-1 on the Au nanoporous surface appear at 530.24 and 531.84 eV, which can be assigned to N=O and C=O–OH, respectively. The shifted N 1s spectrum shows peaks corresponding to C–N, N=O, and the oxide NH₂/NH₃⁺ at 397.70, 399.22, and 402.57 eV, respectively, which strongly indicate the presence of proteins. It shows that greatly influential interactions between protein molecules via amino groups can be found. The S 2p spectrum peak at 167.90 eV can be assigned to SO₄²⁻, which confirms the PTS reaction on the GST-PSGL-1-assembled surface. These peaks are consistent with SAM chemical states. Therefore, there is strong chemisorption between proteins and the Au nanoporous surface. The fabricated protein-assembled substrate surface was used for further SERS studies.

Figure 5 shows the SERS spectra of GST-PSGL-1 and S-GST-PSGL-1 immobilized Au nanoporous substrates obtained at a Raman laser wavelength of 633 nm. The SERS spectra of the APTES-modified functionalized Au nanoporous substrate show weak C–O–C, Si–O–Si, or Si–O–C Raman bands at 813 and 1007 cm⁻¹, respectively, confirming that APTES had self-assembled on the substrate [41].

Notably, the O–C=O stretching modes had significant shifts at 1590–1700 cm^{-1} after the protein was immobilized on the Au nanoporous substrate via the SAM procedure, as marked in Figure 5a.

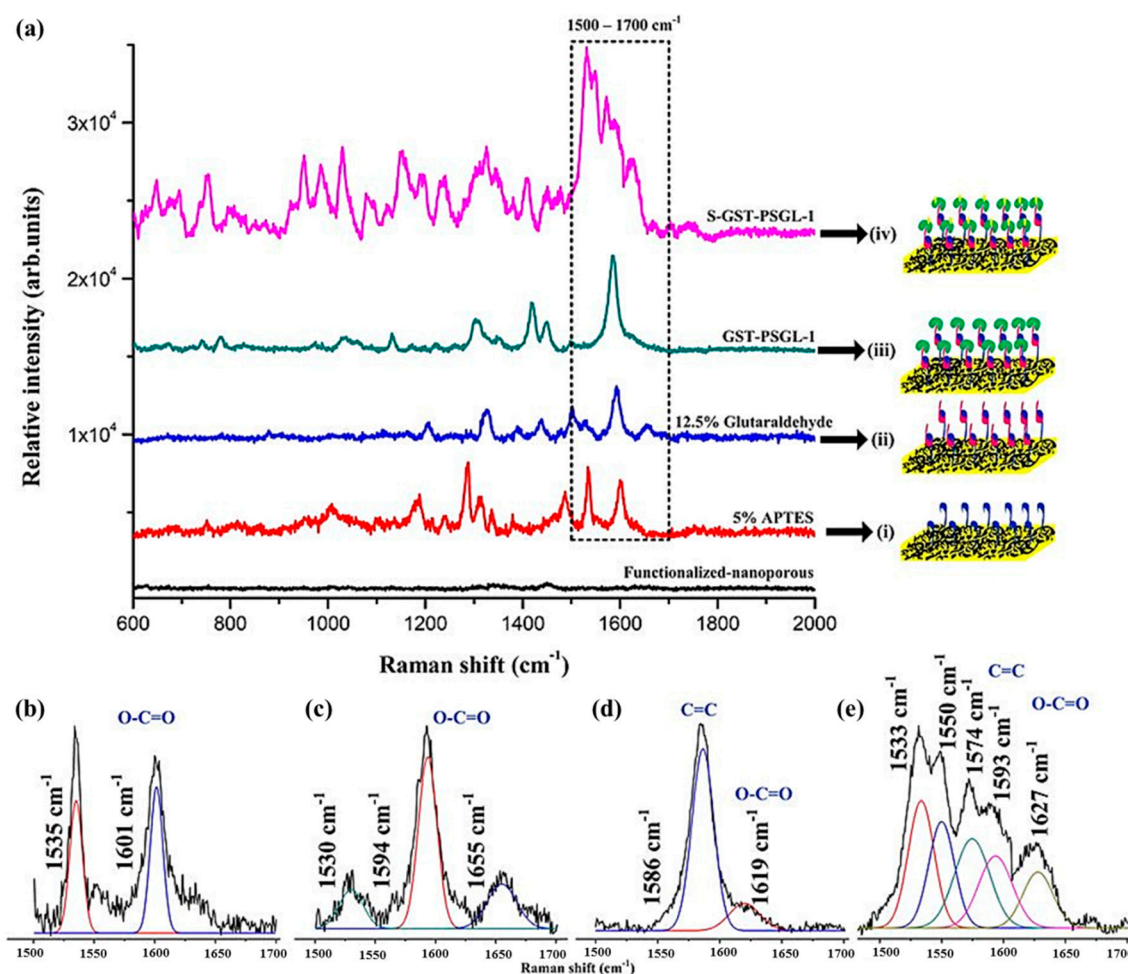


Figure 5. (a) The immobilization of protein on the Au nanoplasmonic substrate. An amino group formed on the functionalized Au nanoporous surface was followed by a self-assembled monolayer (SAM) layer, 3-amino-propyltriethoxysilane (APTES)/ethanol solution, and glutaraldehyde. GST-PSGL-1 or S-GST-PSGL-1 was then immobilized on the SAM-modified Au nanoporous surface. At each step, samples were characterized at a Raman laser wavelength of 633 nm. Marked SERS bands at 1500–1700 cm^{-1} are highlighted. (b) The SERS spectrum of the APTES-modified Au nanoporous substrate shows the O–C=O stretching mode at 1601 cm^{-1} . (c) The glutaraldehyde-modified substrate SERS spectrum shows strongly shifted O–C=O stretching modes at 1594 and 1655 cm^{-1} . (d,e) After the PTS reaction, the observed C=C and O–C=O peaks shifted to 1593 and 1627 cm^{-1} , respectively.

The SERS spectrum of the APTES-modified Au nanoporous substrate shows the O–C=O stretching mode at 1601 cm^{-1} , which is correlated to impurities in the APTES solution, as shown in Figure 5b. The glutaraldehyde-modified substrate SERS spectrum shows strongly shifted O–C=O stretching modes at 1594 and 1655 cm^{-1} , which correspond to glutaraldehyde immobilization, as shown in Figure 5c [42]. The stretching mode of the O–C=O region can greatly influence interactions between protein molecules via amino groups. The SERS spectra of the GST-PSGL-1 modified Au nanoporous substrate show a strong C=C Raman band at 1586 cm^{-1} , confirming the immobilization of GST-PSGL-1 [43–46]. In addition, the stretching mode of O–C=O at 1619 cm^{-1} shifted to a lower region compared to that of the glutaraldehyde-modified Au nanoporous substrates. S-GST-PSGL-1 formed on the Au nanoporous substrates via the PTS reaction. An anionic sulfate is assigned to the asymmetric SO_4^{2-} and $-\text{SO}_3$ stretching modes at 984, 1030, and 1192 cm^{-1} , confirming GST-PSGL-1 modification via the PTS

reaction [27,47]. After the PTS reaction, the observed C=C and O=C=O peaks shifted to 1593 and 1627 cm^{-1} , as shown in Figure 5d,e, respectively, indicating the presence of a protein. The SERS shifts are listed in Table S2. These results are consistent with the XPS results, as detailed in Figure 4.

3.3. Protein-Protein Interactions on the Plasmonic Au Nanoporous Substrate

Figure 6 shows a SERS spectrum of the GST-PSGL-1 mutant's immobilization on an Au nanoporous substrate obtained at a Raman laser wavelength of 633 nm. The SERS band positions were significantly changed due to the various GST-PSGL-1 mutants; these peaks are assigned to proteins, amides, and lipids, as listed in Table S3 [25,26,47–50]. The tyrosine residue positions 46, 48, and 51 of GST-PSGL-1 were positions mutated to phenylalanine (F). Weak phenylalanine SERS bands were observed at 998–1005 cm^{-1} , confirming the presence of the mutant on the surface. Strong SERS peaks appeared at 1595–1650 cm^{-1} , which are related to the O=C=O stretching modes of phenylalanine [44,51]. In addition, a strong anionic sulfate SERS peak appeared at 986 cm^{-1} for the non-mutant GST-PSGL-1. In the case of the GST-PSGL-1 mutant's immobilization on an Au nanoporous substrate, the anionic sulfate SERS peak appeared at 1100–1300 cm^{-1} . A series of the GST-PSGL-1 mutant's O=C=O stretching modes were presenting new and shifted SERS bands at 1591 and 1626 cm^{-1} for (46, 48, 51), 1638 cm^{-1} for (46F), 1622 and 1649 cm^{-1} for (48F), 1595 and 1622 cm^{-1} for (51F), 1626 cm^{-1} for (46F, 48F), 1602 and 1632 cm^{-1} for (46F, 51F), 1592 and 1631 cm^{-1} for (48F, 51F), and 1644 cm^{-1} for (46F, 48F, 51F), which can be used to determine the quality and conformation of the mutated protein. Three regions of the mutated protein (46F, 48F, 51F) on the Au nanoporous substrate showed highly enhanced SERS intensity at 1001 cm^{-1} due to a high quantity of phenylalanine. Furthermore, the SERS relative intensity of the peak positions at 1626–1649 cm^{-1} (O=C=O) were compared to detect the SERS activity of the mutated regions on the Au nanoporous substrate (Figure 6b). The maximum mutated protein SERS intensity (at O=C=O) was reduced compared to that of the control GST-PSGL-1 on the Au nanoporous substrate due to the structure being modified by phenylalanine. Nevertheless, the mutated GST-PSGL-1 positions at 48F, 51F, (46F, 48F), and (46F, 51F) on the Au nanoporous substrate showed greatly enhanced SERS intensity (at O=C=O). These positions could be used to understand interactions with antibodies or VP1 of EV71.

The S-GST-PSGL-1-immobilized Au nanoporous substrate was allowed to interact with anti-sulfotyrosine and examined at a Raman laser wavelength of 633 nm. Figure 6c shows a SERS spectrum of S-GST-PSGL-1 interaction with anti-sulfotyrosine. Strong anionic sulfate SERS bands appeared at 978 and 1282 cm^{-1} , corresponding to stretching modes of SO_4^{2-} , $-\text{SO}_3$, and S=O, which may correspond to the strong interaction between the sulfated protein and the antibody. The major and minor Raman assignments of the protein and antibody were performed in the 600–1800 cm^{-1} range; they are listed in Table S4. The SERS peaks shifted to higher and lower regions due to the chemical configuration of protein interactions with the antibody, as shown in Figure S4 and S5. The non-mutated and mutated GST-PSGL-1 positions at (46, 48, 51), (46F), (48F), (51F), (46F, 48F), (46F, 51F), (48F, 51F), and (46F, 48F, 51F) have higher affinities toward the antibody, which was confirmed by the presence of a SERS band at 978–986 cm^{-1} from anionic sulfate groups. For the mutated GST-PSGL-1 positions at (48F) and (46F, 51F), anionic sulfate group SERS bands shifts appeared at 1100–1300 cm^{-1} , which could be correlated to the specific interaction of mutated protein and antibody. Moreover, the weak SERS characteristic peak of phenylalanine obtained at 997–1000 cm^{-1} indicates the presence of mutated protein on the Au nanoporous substrate. The O=C=O stretching mode appeared at 1599–1666 cm^{-1} . The SERS spectra for all samples shifted to lower or higher regions due to antibody interactions. The relative SERS intensity of the peak positions at 1599–1666 cm^{-1} (O=C=O) were compared to detect SERS activity at mutated regions on the Au nanoporous substrate (Figure S4). The mutated protein positions at (51F) and (48F, 51F) had high peak intensities at 1599–1666 cm^{-1} , which could be related to non-binding with the mutated protein and the antibody. These positions exhibit a strong SERS effect on the Au nanoporous substrate. In addition, the mutated protein positions at (46F), (48F), (46F, 48F), (46F, 51F), and (46F, 48F, 51F) SERS intensity (O=C=O) decreased due to strong binding with the

mutated protein and the antibody. Therefore, the mutated protein positions at (51F) and (48F, 51F) play the most important roles in VP1 interaction.

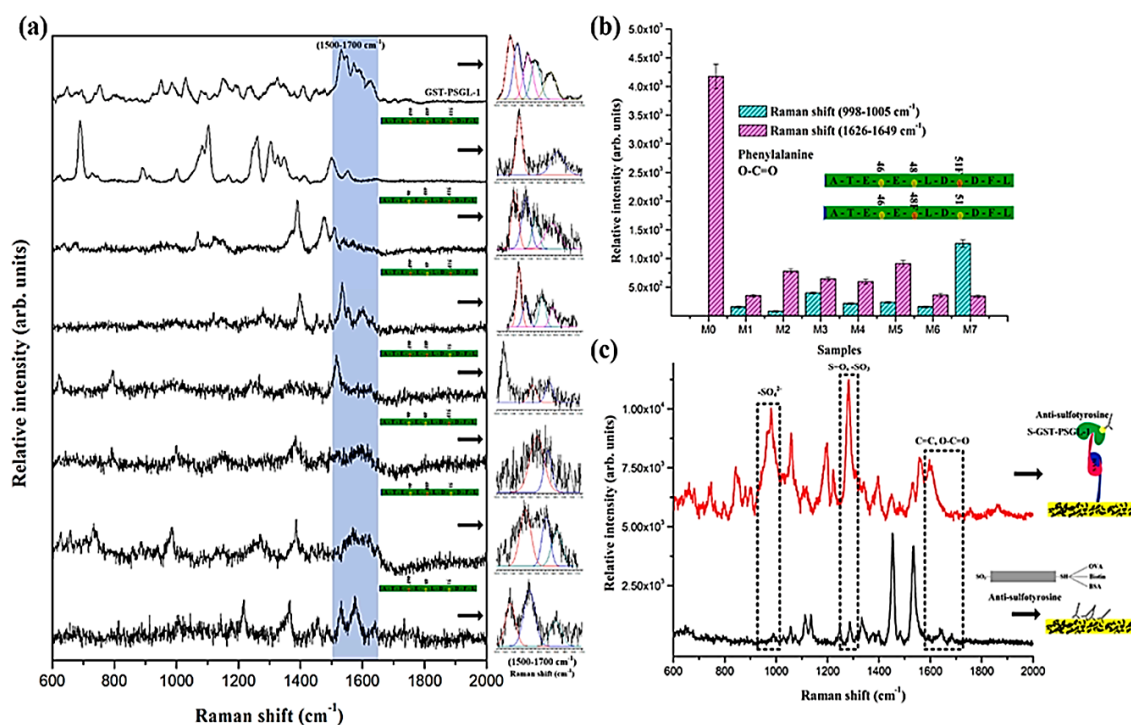


Figure 6. The SERS spectra of the GST-PSGL-1 mutants on the SAM-modified Au nanoporous substrate were examined at a Raman laser wavelength of 633 nm. (a) Marked SERS bands at 1500–1700 cm^{-1} are highlighted. (b) The relationships of relative SERS intensities for the various protein mutants on the Au nanoporous substrate were determined using I_{SERS} peak regions at 998–1005 and 1626–1649 cm^{-1} . (c) The SERS spectra of S-GST-PSGL-1 and antibody-sulfotyrosine interaction on the Au nanoporous substrate were examined at a Raman laser wavelength of 633 nm.

It is known that S-GST-PSGL-1 acts as a mediator between cells and an external virus. The VP1 (1 μm) of EV71 was diluted using PBS solution, with which about 2 mL was taken and immobilized onto the protein-modified samples for 12 h. The mutated GST-PSGL-1 and VP1 of EV71 interaction on the Au nanoporous substrate was examined at a Raman laser wavelength of 633 nm; the results are shown in Figure 7. The major and minor Raman assignments of PPIs were performed in the 600–1800 cm^{-1} range; they correspond to amides, amino acids, and lipids, as listed in Table S5. The strong SERS bands of PPIs (mutated GST-PSGL-1 and VP1) that appear at 1361 cm^{-1} for (46, 48, 51) are assigned to lipids, those at 1121 cm^{-1} for (46F) are assigned to C–C trans-conformation, those at 826 cm^{-1} for (48F) are assigned to NH_2 , those at 1601 cm^{-1} for (51F) are assigned to O–C=O, those at 1139 cm^{-1} for (46F, 48F) are assigned to C–C trans-conformation, those at 1567 cm^{-1} for (46F, 51F) are assigned to amides, those at 838 and 858 cm^{-1} for (48F, 51F) are assigned to NH_2 and lipids, and those at 1131 cm^{-1} for (46F, 48F, 51F) are assigned to C–C trans-conformation [25,26,44,52,53]. The results indicate that the SERS signals were significantly different for each mutated protein interaction with VP1 due to the different structural composition of protein. The SERS characteristic peaks are mostly from VP1, which indicated the binding strength of PPIs. Figure S5 shows the SERS spectra of VP1 dropped on an Au nanoporous substrate. The peaks correspond to the amides, amino acids, and lipids of VP1. Moreover, the SERS relative intensity of the peak position at 1600 cm^{-1} was compared to the detected SERS intensity of PPIs (Figure 7b). The strong SERS intensity of the mutated protein at (48F), (51F), and (46F, 48F) indicates less interaction with VP1 due to the presence of a strong phenylalanine signal from the mutated protein. Therefore, the activity of mutated GST-PSGL-1 at

positions (48F), (51F), and (46F, 48F) may control the path for virus entry, which is consistent with our previous work and detailed in SI. The AFM measurements of S-GST-PSGL-1 mutants and VP1 of EV71, as shown in Figure 7c. Generally, selectin-PSGL-1 interactions depend on the microenvironment of the interacting molecules (molecular structure). PTS-based GST-PSGL-1 may regulate the interaction of VP1 of EV71. The force measurement procedure described in a previous paper was applied in this study. AFM was used to measure the unbinding force between the outer sheath protein VP-1 of EV71 and GST-PSGL-1. Through APTES and glutaraldehyde (GA), the proteins were, respectively, covalently attached on the apex of the AFM tip and silicon substrate. Then, the unbinding forces between the proteins were analyzed. The unbinding force between sulfated-GST-PSGL-1 and VP-1 was obviously stronger than that of nonsulfated-GST-PSGL-1 since the specific bonding between the proteins affects the unbinding force.

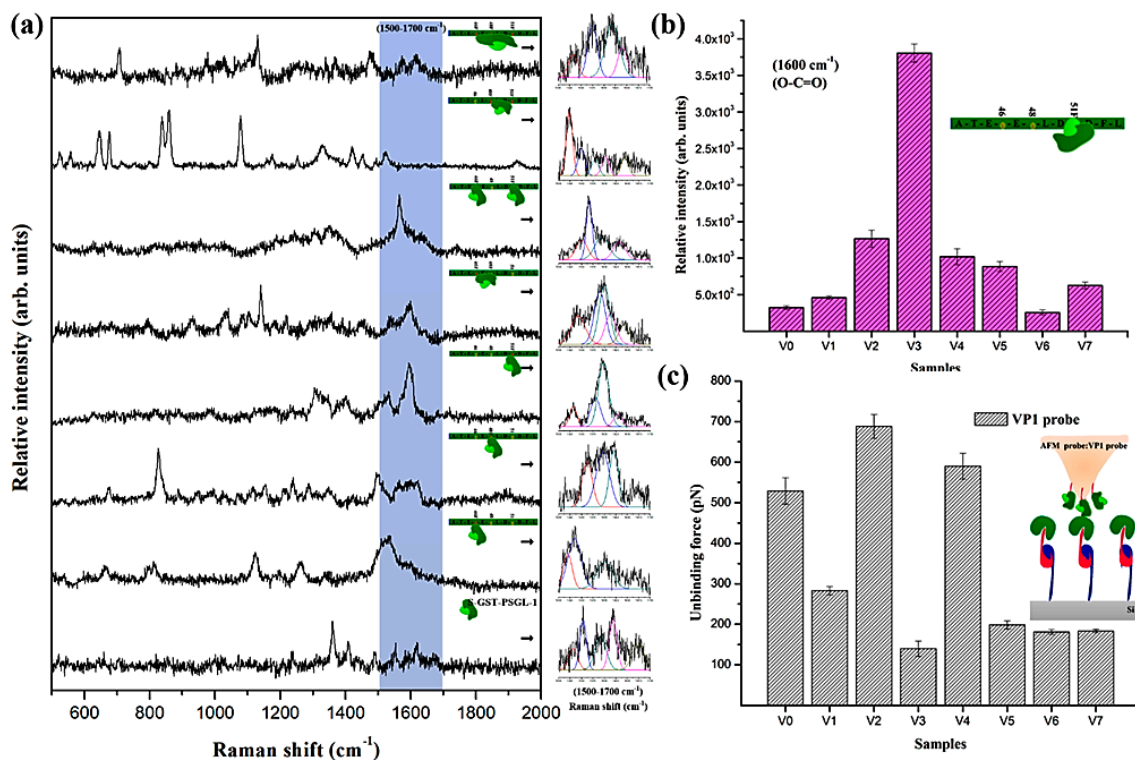


Figure 7. The SERS spectra of GST-PSGL-1 mutant and VP1 proteins of enterovirus 71 (EV71) interactions on the SAM-modified Au nanoporous surface were examined at a Raman laser wavelength of 633 nm. (a) Marked SERS bands at 1500–1700 cm^{-1} are highlighted. (b) The relationships of the relative Raman intensities for various mutant proteins and VP1 interactions on Au nanoporous substrate were determined using the I_{SERS} peak region at 1600 cm^{-1} . (c) The unbinding force of VP1 probe V0–V7.

4. Conclusions

In this study, Au nanoporous SERS-active substrates were utilized for detecting PPIs. Protein immobilization on the Au nanoporous substrate was confirmed using XPS and SERS. The mutated protein SERS effect was investigated through the observation of a strong phenylalanine SERS signal. The mutated protein positions at (51F) and (48F, 51F) exhibited a high SERS effect at 1599–1666 cm^{-1} , which could be related to non-binding with the mutated protein and anti-sulfotyrosine interaction on the Au nanoporous substrate. The stretching mode of O–C=O (phenylalanine) at the 1600 cm^{-1} SERS band was compared to the mutated protein and VP1 interactions. The strong SERS effect of the mutated protein and VP1 interactions was obtained at (48F), (51F), and (46F, 48F); these positions indicated less interaction with VP1 due to the presence of a strong phenylalanine signal from the mutated

protein. The proposed method will help in drug development and contribute to the understanding of physiological and pathological mechanisms.

Supplementary Materials: The following are available online at <http://www.mdpi.com/2079-6412/10/4/403/s1>, Figure S1: Schematic illustration of fabrication of Au nanoporous substrate, Figure S2: HR-FETEM image of optimized Au nanoporous substrate and EDS mappings of areas marked in HR-FETEM image, Figure S3: SPR spectra of as-fabricated Au nanoporous substrate created at deposition rates of (a) 0.3 Å/s and (b) 1 Å/s with optimized dealloying times (120 and 150 s, respectively). (c) COMSOL calculation of smooth and roughed Au nanocavity, Figure S4: Relationship of relative Raman intensities for various mutants and antibody-sulfotyrosine interactions on Au nanoporous substrate determined using ISERS peak regions at 990–1010 and 1601–1636 cm⁻¹, Figure S5: VP1 of EV71 on Au nanoporous substrate examined at Raman laser wavelength of 633 nm, Table S1: Nanopore size and contact angle of as-fabricated Au nanoporous substrates, Table S2: Raman assignment for protein immobilized on Au nanoporous substrate [1–12], Table S3: Raman assignment for protein mutants on Au nanoporous substrate [1–12], Table S4: Raman assignment for protein-antibody interaction on Au nanoporous substrate [1–13], Table S5: Raman assignment for PPIs on Au nanoporous substrate [3–13].

Author Contributions: Conceptualization, K.S.; methodology, Y.-S.Y.; data curation, H.L.; writing—review and editing, H.L., J.-D.L. and J.S.; supervision, J.-D.L.; formal analysis, C.-C.W. and C.-H.L.; software, J.S. All authors have read and agreed to the published version of the manuscript.

Funding: This research received grant from the Headquarter of University Advancement at National Cheng Kung University (NCKU), sponsored by the Taiwan Ministry of Science and Technology under Grant Nos. 108-2218-E-006-054-MY3, 106-2811-E-066-061 and 108-2811-E-006-535.

Acknowledgments: The funder had no role in study design, data collection, and analysis, decision to publish, or preparation of the manuscript.

Conflicts of Interest: The authors declare no conflict of interest.

References

1. Bettelheim, F.R. Tyrosine-O-sulfate in a peptide from fibrinogen. *J. Am. Chem. Soc.* **1954**, *76*, 2838–2839. [[CrossRef](#)]
2. Moore, K.L. The biology and enzymology of protein tyrosine O-sulfation. *J. Biol. Chem.* **2003**, *278*, 24243–24246. [[CrossRef](#)]
3. Kehoe, J.W.; Bertozzi, C.R. Tyrosine sulfation: A modulator of extracellular protein–protein interactions. *Chem. Biol.* **2000**, *7*, R57–R61. [[CrossRef](#)]
4. Huang, B.Y.; Chen, P.C.; Chen, B.H.; Wang, C.C.; Liu, H.F.; Chen, Y.Z.; Chen, C.S.; Yang, Y.S. High-throughput screening of sulfated proteins by using a genome-wide proteome microarray and protein tyrosine sulfation system. *Anal. Chem.* **2017**, *89*, 3278–3284. [[CrossRef](#)]
5. Monigatti, F.; Hekking, B.; Steen, H. Protein sulfation analysis—a primer. *Biochim. Biophys. Acta (BBA) Proteins Proteom.* **2006**, *1764*, 1904–1913. [[CrossRef](#)]
6. Seibert, C.; Sakmar, T.P. Toward a framework for sulfoproteomics: Synthesis and characterization of sulfotyrosine-containing peptides. *Pept. Sci.* **2008**, *90*, 459–477. [[CrossRef](#)]
7. Seibert, C.; Cadene, M.; Sanfiz, A.; Chait, B.T.; Sakmar, T.P. Tyrosine sulfation of CCR5 N-terminal peptide by tyrosylprotein sulfotransferases 1 and 2 follows a discrete pattern and temporal sequence. *Proc. Natl. Acad. Sci. USA* **2002**, *99*, 11031–11036. [[CrossRef](#)]
8. Angiari, S.; Constantin, G. Regulation of T cell trafficking by the T cell immunoglobulin and mucin domain 1 glycoprotein. *Trends Mol. Med.* **2014**, *20*, 675–684. [[CrossRef](#)]
9. Dong, J.F.; Ye, P.; Schade, A.J.; Gao, S.; Romo, G.M.; Turner, N.T.; López, J.A. Tyrosine sulfation of glycoprotein Ib α role of electrostatic interactions in von willebrand factor binding. *J. Biol. Chem.* **2011**, *276*, 16690–16694. [[CrossRef](#)]
10. Farzan, M.; Mirzabekov, T.; Kolchinsky, P.; Wyatt, R.; Cayabyab, M.; Gerard, N.P.; Choe, H. Tyrosine sulfation of the amino terminus of CCR5 facilitates HIV-1 entry. *Cell* **1999**, *96*, 667–676. [[CrossRef](#)]
11. Hsu, W.; Rosenquist, G.L.; Ansari, A.A.; Gershwin, M.E. Autoimmunity and tyrosine sulfation. *Autoimmun. Rev.* **2005**, *4*, 429–435. [[CrossRef](#)]
12. Braun, P.; Gingras, A.C. History of protein–protein interactions: From egg-white to complex networks. *Proteomics* **2012**, *12*, 1478–1498. [[CrossRef](#)]

13. Huang, C.C.; Venturi, M.; Majeed, S.; Moore, M.J.; Phogat, S.; Zhang, M.Y.; Wyatt, R. Structural basis of tyrosine sulfation and VH-gene usage in antibodies that recognize the HIV type 1 coreceptor-binding site on gp120. *Proc. Natl. Acad. Sci. USA* **2004**, *101*, 2706–2711. [[CrossRef](#)]
14. Farzan, M.; Babcock, G.J.; Vasilieva, N.; Wright, P.L.; Kiprilov, E.; Mirzabekov, T.; Choe, H. The role of post-translational modifications of the CXCR4 amino terminus in stromal-derived factor 1 α association and HIV-1 entry. *J. Biol. Chem.* **2002**, *277*, 29484–29489. [[CrossRef](#)]
15. Nishimura, Y.; Shimojima, M.; Tano, Y.; Miyamura, T.; Wakita, T.; Shimizu, H. Human P-selectin glycoprotein ligand-1 is a functional receptor for enterovirus 71. *Nat. Med.* **2009**, *15*, 794. [[CrossRef](#)]
16. Nishimura, Y.; Wakita, T.; Shimizu, H. Tyrosine sulfation of the amino terminus of PSGL-1 is critical for enterovirus 71 infection. *PLoS Pathog.* **2010**, *6*, 1174. [[CrossRef](#)]
17. Chen, B.H.; Wang, C.C.; Lu, L.Y.; Hung, K.S.; Yang, Y.S. Fluorescence assay for protein post-translational tyrosine sulfation. *Anal. Bioanal. Chem.* **2013**, *405*, 1425–1429. [[CrossRef](#)]
18. Goldberg, M.E.; Djavadi-Ohanian, L. Methods for measurement of antibody/antigen affinity based on ELISA and RIA. *Curr. Opin. Immunol.* **1993**, *5*, 278–281. [[CrossRef](#)]
19. Robinson, M.R.; Moore, K.L.; Brodbelt, J.S. Direct identification of tyrosine sulfation by using ultraviolet photodissociation mass spectrometry. *J. Am. Soc. Mass Spectrom.* **2014**, *25*, 1461–1471. [[CrossRef](#)]
20. Itkonen, O.; Helin, J.; Saarinen, J.; Kalkkinen, N.; Ivanov, K.I.; Stenman, U.H.; Valmu, L. Mass spectrometric detection of tyrosine sulfation in human pancreatic trypsinogens, but not in tumor-associated trypsinogen. *FEBS J.* **2008**, *275*, 289–301. [[CrossRef](#)]
21. Wang, C.C.; Sivashanmugan, K.; Chen, C.K.; Hong, J.R.; Sung, W.I.; Liao, J.D.; Yang, Y.S. Specific unbinding forces between mutated human P-selectin glycoprotein ligand-1 and viral protein-1 measured using force spectroscopy. *J. Phys. Chem. Lett.* **2017**, *8*, 5290–5295. [[CrossRef](#)]
22. Pence, I.; Mahadevan-Jansen, A. Clinical instrumentation and applications of Raman spectroscopy. *Chem. Soc. Rev.* **2016**, *45*, 1958–1979. [[CrossRef](#)]
23. Sato, H.; Maeda, Y.; Ishigaki, M.; Andriana, B.B. Biomedical Applications of Raman Spectroscopy. In *Encyclopedia of Analytical Chemistry: Applications, Theory and Instrumentation*; John Wiley & Sons, Inc.: Hoboken, NJ, USA, 2006; pp. 1–12.
24. Luo, S.C.; Sivashanmugan, K.; Liao, J.D.; Yao, C.K.; Peng, H.C. Nanofabricated SERS-active substrates for single-molecule to virus detection in vitro: A review. *Biosens. Bioelectron.* **2014**, *61*, 232–240. [[CrossRef](#)]
25. Sivashanmugan, K.; Huang, W.L.; Lin, C.H.; Liao, J.D.; Lin, C.C.; Su, W.C.; Wen, T.C. Bimetallic nanoplasmonic gap-mode SERS substrate for lung normal and cancer-derived exosomes detection. *J. Taiwan Inst. Chem. Eng.* **2017**, *80*, 149–155. [[CrossRef](#)]
26. Sivashanmugan, K.; Liao, J.D.; You, J.W.; Wu, C.L. Focused-ion-beam-fabricated Au/Ag multilayered nanorod array as SERS-active substrate for virus strain detection. *Sensors Actuat. B Chem.* **2013**, *181*, 361–367. [[CrossRef](#)]
27. Sivashanmugan, K.; Liu, P.C.; Tsai, K.W.; Chou, Y.N.; Lin, C.H.; Chang, Y.; Wen, T.C. An anti-fouling nanoplasmonic SERS substrate for trapping and releasing a cationic fluorescent tag from human blood solution. *Nanoscale* **2017**, *9*, 2865–2874. [[CrossRef](#)]
28. Pallaoro, A.; Mirsafavi, R.Y.; Culp, W.T.; Braun, G.B.; Meinhart, C.D.; Moskovits, M. Screening for canine transitional cell carcinoma (TCC) by SERS-based quantitative urine cytology. *Nanomed. Nanotechnol. Biol. Med.* **2018**, *14*, 1279–1287. [[CrossRef](#)]
29. Wang, H.N.; Fales, A.M.; Vo-Dinh, T. Plasmonics-based SERS nanobiosensor for homogeneous nucleic acid detection. *Nanomed. Nanotechnol. Biol. Med.* **2015**, *11*, 811–814. [[CrossRef](#)]
30. Kumar, S.; Kumar, A.; Kim, G.H.; Rhim, W.K.; Hartman, K.L.; Nam, J.M. Myoglobin and polydopamine-engineered raman nanoprobe for detecting, imaging, and monitoring reactive oxygen species in biological samples and living cells. *Small* **2017**, *13*, 1701584. [[CrossRef](#)]
31. Shin, S.; Lee, J.; Lee, S.; Kim, H.; Seo, J.; Kim, D.; Lee, T. A droplet-based high-throughput SERS platform on a droplet-guiding-track-engraved superhydrophobic substrate. *Small* **2017**, *13*, 1602865. [[CrossRef](#)]
32. Xue, L.; Xie, W.; Driessen, L.; Domke, K.F.; Wang, Y.; Schlücker, S.; Steinhart, M. Advanced SERS sensor based on capillarity-assisted preconcentration through gold nanoparticle-decorated porous nanorods. *Small* **2017**, *13*, 1603947. [[CrossRef](#)]
33. Arnob, M.M.P.; Zhao, F.; Zeng, J.; Santos, G.M.; Li, M.; Shih, W.C. Laser rapid thermal annealing enables tunable plasmonics in nanoporous gold nanoparticles. *Nanoscale* **2014**, *6*, 12470–12475. [[CrossRef](#)]

34. Seker, E.; Reed, M.L.; Begley, M.R. Nanoporous gold: Fabrication, characterization, and applications. *Materials* **2009**, *2*, 2188–2215. [[CrossRef](#)]
35. Polat, O.; Seker, E. Effect of surface–molecule interactions on molecular loading capacity of nanoporous gold thin films. *J. Phys. Chem. C* **2016**, *120*, 19189–19194. [[CrossRef](#)]
36. Ke, X.; Xu, Y.; Yu, C.; Zhao, J.; Cui, G.; Higgins, D.; Wu, G. Pd-decorated three-dimensional nanoporous Au/Ni foam composite electrodes for H₂O₂ reduction. *J. Mater. Chem. A* **2014**, *2*, 16474–16479. [[CrossRef](#)]
37. Dorofeeva, T.S.; Seker, E. In situ electrical modulation and monitoring of nanoporous gold morphology. *Nanoscale* **2016**, *8*, 19551–19556. [[CrossRef](#)]
38. Ishida, S.; Anno, Y.; Takeuchi, M.; Matsuoka, M.; Takei, K.; Arie, T.; Akita, S. Highly photosensitive graphene field-effect transistor with optical memory function. *Sci. Rep.* **2015**, *5*, 15491. [[CrossRef](#)]
39. Kim, W.K.; Lee, J.L. Effect of oxygen plasma treatment on reduction of contact resistivity at pentacene/Au interface. *Appl. Phys. Lett.* **2006**, *88*, 262102. [[CrossRef](#)]
40. Liu, W.; Sun, D.; Fu, J.; Yuan, R.; Li, Z. Assembly of evenly distributed Au nanoparticles on thiolated reduced graphene oxide as an active and robust catalyst for hydrogenation of 4-nitroarenes. *RSC Adv.* **2014**, *4*, 11003–11011. [[CrossRef](#)]
41. Pasternack, R.M.; Rivillon, A.S.; Chabal, Y.J. Attachment of 3-(aminopropyl) triethoxysilane on silicon oxide surfaces: Dependence on solution temperature. *Langmuir* **2008**, *24*, 12963–12971. [[CrossRef](#)]
42. Jastrzebska, M.; Wrzalik, R.; Kocot, A.; Zalewska-Rejdak, J.; Cwalina, B. Raman spectroscopic study of glutaraldehyde-stabilized collagen and pericardium tissue. *J. Biomater. Sci. Polym. Ed.* **2003**, *14*, 185–197. [[CrossRef](#)]
43. Satheeshkumar, E.; Karuppaiya, P.; Sivashanmugan, K.; Chao, W.T.; Tsay, H.S.; Yoshimura, M. Biocompatible 3D SERS substrate for trace detection of amino acids and melamine. *Pectroc. Acta Pt. A-Molec. Biomolec. Spectr.* **2017**, *181*, 91–97. [[CrossRef](#)]
44. Madzharova, F.; Heiner, Z.; Kneipp, J. Surface enhanced hyper-Raman scattering of the amino acids tryptophan, Histidine, Phenylalanine, and Tyrosine. *J. Phys. Chem. C* **2017**, *121*, 1235–1242. [[CrossRef](#)]
45. Hernández, B.; Coïc, Y.M.; Pflüger, F.; Kruglik, S.G.; Ghomi, M. All characteristic Raman markers of tyrosine and tyrosinate originate from phenol ring fundamental vibrations. *J. Raman Spectrosc.* **2016**, *47*, 210–220. [[CrossRef](#)]
46. Fischer, W.B.; Eysel, H.H. Polarized Raman spectra and intensities of aromatic amino acids phenylalanine, tyrosine and tryptophan. *Spectroc. Acta Pt. A-Molec. Biomolec. Spectr.* **1992**, *48*, 725–732. [[CrossRef](#)]
47. Bugaev, K.O.; Zelenina, A.A.; Volodin, V.A. Vibrational spectroscopy of chemical species in silicon and silicon-rich nitride thin films. *J. Spectrosc.* **2012**, *2012*, 281851. [[CrossRef](#)]
48. Li, Y.T.; Li, D.W.; Cao, Y.; Long, Y.T. Label-free in-situ monitoring of protein tyrosine nitration in blood by surface-enhanced Raman spectroscopy. *Biosens. Bioelectron.* **2015**, *69*, 1–7. [[CrossRef](#)]
49. Brewster, V.L.; Ashton, L.; Goodacre, R. Monitoring the glycosylation status of proteins using Raman spectroscopy. *Anal. Chem.* **2011**, *83*, 6074–6081. [[CrossRef](#)]
50. Davies, H.S.; Singh, P.; Deckert-Gaudig, T.; Deckert, V.; Rousseau, K.; Ridley, C.E.; Blanch, E.W. Secondary structure and glycosylation of mucus glycoproteins by Raman spectroscopies. *Anal. Chem.* **2016**, *88*, 11609–11615. [[CrossRef](#)]
51. Ravikumar, B.; Rajaram, R.K.; Ramakrishnan, V. Raman and IR spectral studies of L-phenylalanine L-phenylalaninium dihydrogenphosphate and DL-phenylalaninium dihydrogenphosphate. *J. Raman Spectrosc.* **2006**, *37*, 597–605. [[CrossRef](#)]
52. Arp, Z.; Autrey, D.; Laane, J.; Overman, S.A.; Thomas, G.J. Tyrosine Raman signatures of the filamentous virus Ff are diagnostic of non-hydrogen-bonded phenoxyls: Demonstration by Raman and infrared spectroscopy of p-cresol vapor. *Biochemistry* **2001**, *40*, 2522–2529. [[CrossRef](#)] [[PubMed](#)]
53. Li, X.; Martin, S.J.; Chinoy, Z.S.; Liu, L.; Rittgers, B.; Dluhy, R.A.; Boons, G.J. Label-free detection of glycan–protein interactions for array development by surface-enhanced Raman spectroscopy (SERS). *Chem.-Eur. J.* **2016**, *22*, 11180–11185. [[CrossRef](#)] [[PubMed](#)]

